Available online at www.sciencedirect.com
ScienceDirect
Thermochimica Acta 461 (2007) 82–87
thermochimica acta
www.elsevier.com/locate/tca

Size-dependent melting and supercooling of Ge nanoparticles embedded in a SiO_2 thin film

A.F. Lopeandía, J. Rodríguez-Viejo *

Grupo de Nanomateriales y Microsistemas, Departamento de Física, Universidad Autònoma de Barcelona, 08193 Bellaterra, Spain

Available online 12 April 2007

Abstract

Melting of Ge nanocrystals embedded in a 20 nm SiO_2 film is analyzed using a highly sensitive nanocalorimetric technique. Fast heating rates of $\sim 5 \times 10^4$ K/s between room temperature and 1200 K and cooling rates of 8×10^3 K/s at the onset of solidification are used to probe the phase transitions. A melting point reduction of 125 K with respect to the bulk melting temperature is observed upon heating. A size-dependent supercooling has also been observed with an onset of solidification that ranges from 890 to 935 K depending on the maximum size of the previously melted nanoparticles. For a given nanocrystal size the melting hysteresis is around 225 K.

Keywords: Ge nanoparticles; Fast scanning nanocalorimetry; Melting and solidification; Size-dependent supercooling

1. Introduction

Ge nanocrystals embedded in SiO_2 are the object of intense research due to their potential applications in the development of optoelectronic devices or non-volatile memories [1,2]. A promising way to create these nanoparticles is by high temperature annealing of a thin amorphous Ge film sandwiched between SiO_2 layers. During the annealing treatment, typically carried out by rapid thermal annealing or laser processing [3,4], phase transitions such as melting, crystallization and solidification of the amorphous or nanocrystalline phases are often found [5]. Therefore, the ability to obtain a suitable distribution of nanocrystals with a specific size relies on a deep knowledge of the kinetics and thermodynamics involved in the nucleation and growth process. It is well known that phase transitions in nanoscale materials can dramatically change relative to their bulk behavior, because of the large surface-to-volume ratio. The melting depression [6] associated to size-dependent phenomena has been described in many systems [7–10]. Several models have been proposed to describe how a nanoparticle melts. In general, they predict an inverse dependence of the melting temperature with the radius of the particle and $\Delta T(r)$ is proportional to α/r. The various models differ in the parameter α which involves the interfacial energies between the solid phase and the surroundings and the solid and liquid densities. The Homogeneous Melting Model (HMM) is the most used and assumes that at a given temperature the particle melts at once. In this model, the parameter α is $\alpha_{HMM} = \sigma_{SV} - \sigma_{LV}(\rho_S/\rho_L)^{2/3}$ [11]. The melting models are based on thermodynamic arguments and do not include possible kinetic effects related to rapid heating. On the other hand, superheating is a scarce phenomenon that can be found in nanoparticles embedded in a material of a higher melting point but supercooling is routinely observed in most materials. For superheating to occur above the equilibrium melting temperature at low to moderate heating rates it is often necessary to have lattice matching at the interface between the particle and the matrix. When nanoparticles are embedded randomly in a high-T_m matrix a depression of melting temperature is also typically observed in analogy to the behavior of freestanding nanoparticles [12], although the particular melting temperature depends on the nature of the particle/matrix interface. Concerning Ge, past studies have corroborated that freestanding nanocrystalline Ge also experience melting depression [13,14]. However, a recent TEM analysis of Ge nanoparticles embedded in a SiO_2 matrix shows the existence of a large hysteresis around the bulk melting temperature [15]. The authors interpret it from the modified surface free energy between the silicon dioxide matrix and the Ge particle.

The study of phase transitions at the nanoscale by calorimetry demands the refinement of conventional tools. The development of the Si microfabrication techniques has paved the possibility to build up a new family of thin film membrane-based devices

* Corresponding author. Tel.: +34 93 5811769; fax: +34 93 5812155.
E-mail address: javier.rodriguez@uab.es (J. Rodríguez-Viejo).

0040-6031/$ – see front matter © 2007 Elsevier B.V. All rights reserved.
doi:10.1016/j.tca.2007.04.010

[16] that can be used as nanocalorimetric sensors because of the low thermal mass. Pioneering work by Denlinger et al. [17] was at the origin of developments in the field. The membrane, usually a dielectric material like Si_xN_y, serves as an ideal holder to deposit all the necessary elements for calorimetry: heaters, sensors and sample. Under this configuration, several high sensitive calorimeters have been designed [18–21]. Ultrafast thin film calorimetry has been used to monitor size-dependent melting of metallic nanoparticles [19] and vitreous transitions in polymer thin films or single crystals [20,22].

In this paper, we present nanocalorimetric measurements at fast heating rates, $\sim 5 \times 10^4$ K/s, on a sample of Ge nanocrystals embedded within a 20 nm SiO_2 film. The high sensitivity of the technique is well suited to probe melting and solidification transitions during heating and cooling cycles in the temperature range from room temperature to 1200 K.

2. Experimental

2.1. Nanocalorimeter and operation

The sensors were fabricated at the clean room facilities of the Instituto de Microelectrónica de Barcelona IMB-CNM, with standard microfabrication techniques. Details about the procedure and the thermoelectrical stability of the design are presented elsewhere [23]. The nanocalorimeter consists on a freestanding 180 nm low stressed Si_xN_y membrane supported by a silicon frame. A thin 100 nm Pt heater capped with 150 nm of Al_2O_3 is patterned on top of the membrane. The non-symmetric serpentine shape of the heater has been optimized with respect to previous heater designs [24] in order to improve the temperature profile in the sensing area under high heating rate experiments. When a constant current pulse is applied through the resistive element the calorimetric cell (CC) is heated by Joule effect. The Pt thin film also acts as a temperature sensor since previously the temperature coefficient of resistance is obtained by calibration. The voltage drop in the CC is measured as a function of time using a four probe configuration and the $T(R)$ relationship is used to calculate the $T(t)$.

The small heat capacity of the addenda (below 1 μJ/K at room temperature) enables heating rates in the range of 5×10^4 to 10^5 K/s by applying short pulses (∼ms) of current (∼40 mA) in a high vacuum environment (10^{-6} mbars). As already shown by Allen and co-workers [18], at moderate temperatures the system behaves quasi-adiabatically and the heat capacity of the calorimetric cell can be directly calculated from the input power: $C_p[T(t)] = P(t)/\beta(t)$, where β is the heating rate. Improved sensitivity is achieved in differential measurements between two identical sensors. We use two calorimetric cells connected in a series circuit (Fig. 1a) and measure the voltage drop in each one and the differential voltage (ΔV), i.e. the voltage drop in the sample CC (V_{SCC}) minus the voltage drop in the reference CC (V_{RCC}), after amplification. The difference in heat capacity, at moderate temperatures, between the calorimetric cells is proportional to the first derivate of ΔV with time [25]. Therefore, a first order transition should appear as a peak in the $d\Delta V/dt$ data with the onset at the transition temperature. At high temperatures radiation losses are important and the system is far from adiabaticity. In this case, the knowledge of $d\Delta V/dt$ alone does not allow calculation of the true heat capacity, though provides the transformation temperatures. A detailed analysis of the influence of heat losses on the calorimetric measurements will be further described in a forthcoming paper.

2.2. Experimental setup

A pair of twin nanocalorimeters is mounted inside an UHV e-beam evaporation chamber. The calorimeters are placed into a

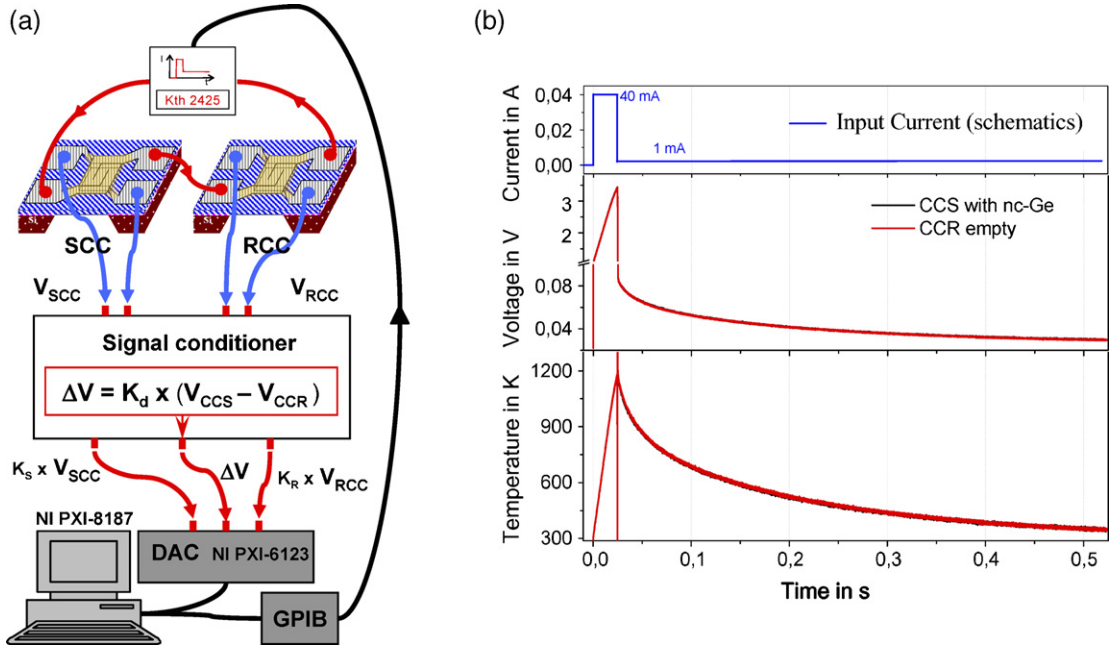

Fig. 1. (a) Schematics of the two calorimetric cells and the electronics used for the measurements. (b) Current pulses and the corresponding voltage and temperature measurements on the calorimetric cell as a function of time.

custom built probe with gold pogopins that electrically connect both devices. Several shutters permit to select the nanocalorimeter to be deposited. A shadow mask defined by photolithography and etching is attached to the bottom of the silicon frame limiting the sample growth to the sensing area of the calorimetric cell. With all these elements, in situ calorimetric measurements are carried out. Fig. 1a shows a schematics of the electronic setup. The calorimetric scan is initiated by applying a short (few ms) dc current pulse of 40 mA through the metallic heater/sensor. The current pulse is followed by a continuous current of 1 mA to monitor the cooling process as shown in Fig. 1b. The signal-to-noise ratio worsens by a factor of 40 with respect to heating but it is still acquired with enough resolution to follow the transformation in the ΔV values, which will also appear as a peak in the $d\Delta V/dt$ signal. The voltage drop in each calorimetric cell is measured in four-probe configuration at 50 kHz with a DAC (NI PXI 6123). Both voltages, V_{SCC} for the sample calorimetric cell and V_{RCC} for the reference calorimetric cell, are acquired after a signal-conditioning step based on instrumentation amplifiers. The ΔV signal is generated after amplification by a factor of 210. The complete system is synchronized by a NI PXI-8187 module that controls the current source (via GPIB) and also the DAC.

Temperature calibration above 500 °C in the same chip is difficult to realize. We then proceed as follows: first, we cycle the microchips under vacuum conditions by locally heating with a dc electrical pulse to the temperature of the experiments. Secondly, we calibrate every microchip in an independent vacuum furnace where the entire sensor is uniformly heated, including the Si frame up to 500 K. From this measurement we determine the temperature coefficient of resistance (TCR) of the heater/sensor, which is typically highly linear up to this temperature with average values around 0.00023–0.0024. We also calibrate several chips of the same wafer by depositing 40 nm thick Ni and Al films, and measuring the Curie temperature and the melting onset, respectively. From these values we determine the non-linear components associated to a given alpha, which we extrapolate to the high temperature region. Finally, for a specific nanocalorimetric experiment we use a heater/sensor with an alpha that matches the TCR of a fully calibrated microchip and assume they exhibit the same high temperature behavior. Using this procedure we estimate a temperature error below 20 K at temperatures in the vicinity of 1100 K. Fig. 2 shows the melting of a 40 nm Al film at different heating rates. The anisotropy of the melting peak observed for the slower rates originates from significant thermal nonuniformities. As the rate increases the melting peak shape improves which confirms the serpentine-type heater is more suited at fast heating rates. A FWHM of 23 K at 1100 K shows the overall goodness of the design at fast rates. The other significant information that can be extracted from this figure is the small change of the onset of melting, about 3 K, induced by different heating rates ranging from 1×10^4 to 5×10^4 K/s. This variation is due to small nonuniformities in the sample region. It is expected, however, that at higher temperatures heat losses through radiation will reduce temperature differences since the regions with higher temperatures will have stronger losses than regions with lower temperatures. This point has been confirmed by thermal modeling [26].

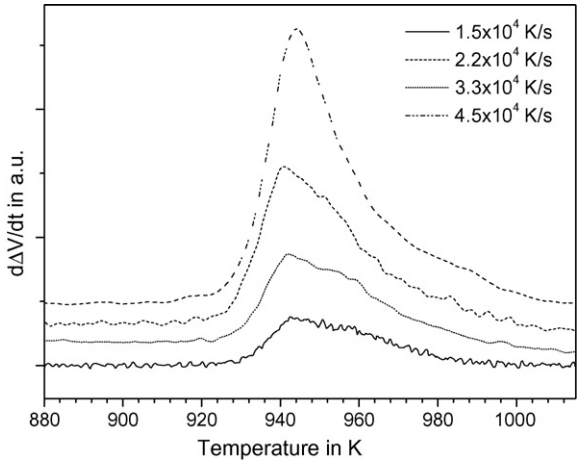

Fig. 2. The derivative of the differential voltage with time as a function of temperature at four different heating rates for a 40 nm Al layer. The curves are vertically shifted for clarity.

2.3. Sample deposition of a-Ge and formation of Ge nanoparticles

In a first step, a buffer SiO_2 layer with a nominal thickness of 10 nm is deposited on both calorimetric cells. The mass evaporated is estimated by a previously calibrated crystal quartz monitor (CQM). A high number of calorimetric scans are performed from room temperature up to 1200 K. These curves show a monotonic rise in temperature and serve as the baseline for subsequent analysis. In a second step, 3 nm of a-Ge are deposited in the SCC. To obtain an amorphous Ge structure the SCC cell is maintained at room temperature and the growth rate fixed to 0.1 nm/s. SiO_2 is a well-known inhibitor of the heterogeneous nucleation of Ge at the interface and previous work has shown that under these conditions the as-deposited Ge is fully amorphous [27]. The shutter is then opened again and an identical capping SiO_2 layer of 10 nm thickness is deposited in both CC. The final structure of the sample in the SCC is a SiO_2/Ge/SiO_2 trilayer. Upon fast heating up to 1200 K the metastable disordered phase melts and during cooling the sample nanocrystallizes [27]. TEM images confirm the diamond like structure of the Ge nanocrystals.

3. Results and discussion

Once the sample is nanocrystallized the first calorimetric scan was performed up to 1170 K. Fig. 1b shows the voltage and temperature curves for both calorimetric cells generated by a pulse of 40 mA during 23.4 ms and the cooling with a current of 1 mA. Plotting the amplified (×210) ΔV signal, black line in Fig. 3, it is possible to appreciate a change in the slope during heating in the range from 21 to 23 ms. This feature is related to the melting of Ge nanoparticles. During cooling another change in slope is observed between 45 and 50 ms, due to solidifica-

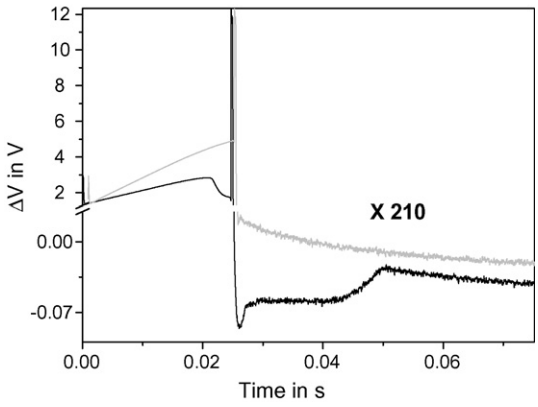

Fig. 3. Differential voltage beween sample and reference calorimetric cells as a function of time. The gray curve represents the data obtained before growth of the 3 nm Ge layer. The black curve corresponds to the temperature increase after formation of the nanocrystals. The slope changes are related to melting and solidification of the Ge nanoparticles.

tion of the previously melted Ge nanoparticles. In Fig. 3, we also plot the ΔV signal of the initial difference between the calorimetric cells, gray curve, to show the baseline of the ΔV evolution without sample. After 20 identical and consecutive scans up to 1170 K the signal was unchanged and therefore we assume the existence of a stable distribution of nanoparticles. The micro-Raman spectrum exhibits a sharp peak at 296 cm^{-1} associated to the optical Raman mode of nanocrystallized Ge. The absence of a Si–Ge phonon mode reflects no interdiffusion and mixing in spite of the high temperatures. To determine the range of particle size that corresponds to the calorimetric scan, ex situ AFM is realized after the nanocalorimetric experiment. The background is removed by image threshold and subsequently the images are analyzed to determine the projected area of each particle. As the calorimetric signal of melting is proportional to the volume the size distribution is multiplied by the volume of every particle for each radius. Fig. 4 shows the existence of a bimodal volume distribution of nanocrystals.

The smaller distribution covers particle sizes between 5 and 15 nm of radii with an average value around 11 nm and a FWHM of 2 nm and the second mode is a Gaussian distribution centered in particle radii around 26 nm with a FWHM of 7 nm.

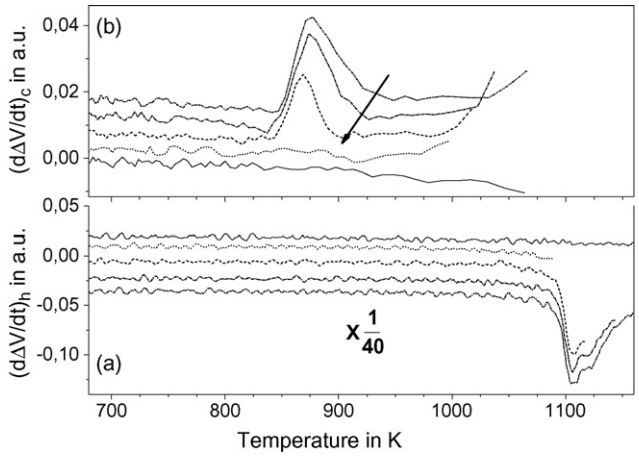

Fig. 5. The derivative of the differential voltage with time as a function of temperature. (a) Measurements during heating: pulses of different duration are injected to probe a different population of nanocrystals. (b) Measurements during cooling of the different heat treatments shown in (a). The continuous line in both graphs is obtained from the empty cells. The arrow marks the temperature variation of the onset of solidification. The curves are vertically shifted for clarity.

3.1. Melting of Ge nanoparticles

The different curves in Fig. 5a show the derivative of the differential voltage with time, $d\Delta V/dt$, obtained during heating with pulses of different widths. This signal provides information of the phase transitions occurring in the sample. The derivative process is typically very noisy and as the typical time scales of the thermal phase transformation in the sample are in the millisecond range box averaging can be applied. Initially, a box of 10 points is used in the original ΔV signal and after differentiation a box of 5 points in the $d\Delta V/dt$ signal. The black line shows the characteristic $d\Delta V/dt$ signal, when the SCC is empty. The endothermic peak of the bottom curve of Fig. 5a, negative $d\Delta V/dt$ signal, corresponds to the melting of the smaller distribution mode of Ge nanoparticles. The onset of the peak at 1090 K marks a clear depression of 125 K below the expected value for bulk Ge. The FWHM of the peak is around 30 K and it is related to both the size distribution of nanoparticles, and the temperature differences in the calorimetric cells. The other curves probing the structure up to lower temperatures, correspond to incomplete melting, i.e. only those nanoparticles below

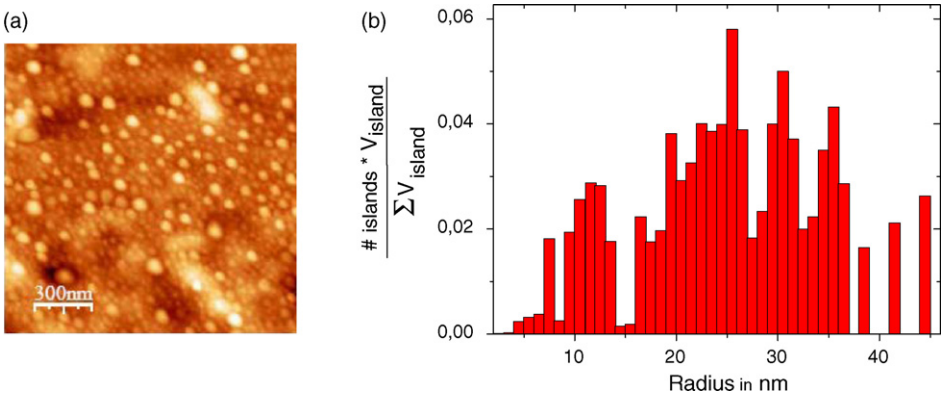

Fig. 4. AFM image obtained in tapping mode (a) and volume distribution of the nanoparticles after heating to 1200 K (b).

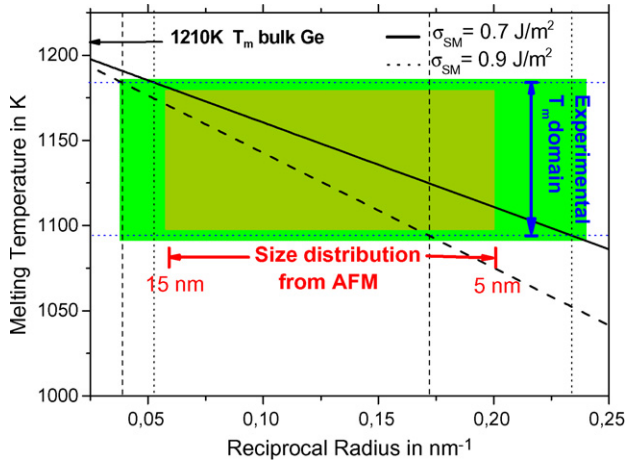

Fig. 6. Melting temperature as a function of the reciprocal radius deduced from the HMM model for the two values of the solid Ge–SiO_2 matrix surface energy. The dash and dotted vertical lines indicate the radius range for the experimentally observed melting temperatures through the HMM model for both values of surface energy.

a given radii are melted. Contrary to recent experimental evidence of superheating above the bulk melting temperature in Ge nanocrystals embedded in a SiO_2 matrix [15] we do observe a depression of the melting temperature with respect to the bulk material. Although both particles are Ge nanocrystals embedded in SiO_2 the preparation method differs greatly and may explain the different behavior. In our case, the nanocrystals are embedded within a thin film of SiO_2 which does not introduce compressive stresses in the Ge nanocrystals as we have already probed by micro-Raman analysis [27]. In the case of the work of Xu et al. [15] pressure build up at the nanoparticles may play a non-negligible role in the observed anomalous superheating.

The observed melting temperature has been compared with predictions from the HMM model using parameters extracted from the literature, latent heat of fusion, $L = 510$ J/g [28], surface energy for the liquid Ge–SiO_2 matrix, $\sigma_{LM} = 0.15$ J/m^2 [29], and for the solid Ge–SiO_2 matrix, $\sigma_{SM} = 0.7$–0–9 J/m^2 [15]. Fig. 6 shows the results obtained as a function of r^{-1} for the two values of the solid nanoparticle-matrix surface energy. The experimentally measured temperatures are represented by the vertical bar and the nanoparticle sizes measured by AFM by the horizontal bar. Our data fall within the limit range predicted by the HMM model, excluding at least in principle the presence of superheating with respect to the equilibrium melting temperature for every size. Nevertheless, the uncertainty in some of the parameters entering the model renders difficult an unambiguous interpretation about the melting process. Superheating of the nanocrystals due to melting kinetics during the rapid heating of our experiments (5×10^4 K/s) also appears to be insignificant in these nanoparticles. An approximation of the sizes melted can be assumed directly confronting the melting peak and the size distribution of the nanoparticles. Within the HMM model we estimate the maximum nanoparticle size that is melted in each scan. Heating up to 1170 K (bottom curve) nanoparticles from 5 to 15 nm are melted, whereas for the next two curves in Fig. 5a the maximum sizes melted are 9 and 12 nm, respectively.

3.2. Solidification and size-dependent supercooling of Ge nanoparticles

The upper curve of Fig. 5b shows the exothermic peak present in $d\Delta V/dt$ upon cooling. The peak corresponds to the solidification of the melted nanoparticles due to previous heating up to 1170 K. The signal-to-noise ratio of the ΔV data during cooling is 40 times smaller than during heating. Given this fact an extra box averaging of 20 points was performed with special care as to avoid manipulation artifacts. The cooling rate at the point of solidification was near 8000 K/s. From Fig. 5b, a dependence of the solidification temperature with the previous heating is observed. By inspection of the solidification curves, obtained after partial melting to different nanocrystal sizes, we demonstrate the occurrence of size-dependent supercooling in the Ge nanoparticles. The onset of solidification appears at 895, 920 and 935 K for samples heated to 1120, 1140 and 1170 K, respectively. For a given nanocrystal size a hysteresis of around 220–230 K with respect to the melting temperature is observed. The size-dependent supercooling can be understood from the temperature dependence of the critical size necessary for solidification. Since the critical radius depends on the supersaturation, the lower the temperature the smaller the critical grain size. Using different current pulses we probe the melting of a reduced population of nanocrystals, the shorter the pulse the lower the temperature reached and therefore only the smaller nanocrystals undergo the solid-to-liquid transition. Solidification of a given liquid particle can only occur if the critical grain size is below the radius of the particle and the solid grain can fit within the liquid. Therefore, for the smaller particles a lower temperature is needed for solidification.

4. Conclusions

We have reported the experimental observation of the size-dependent melting and size-dependent supercooling of a population of Ge nanocrystals with an average radii of 10 nm embedded within a 20 nm SiO_2 film. The incoherent interface between Ge and the SiO_2 matrix inhibits the existence of a large superheating. However, the onset temperature of solidification exhibits a significant supercooling that depends on the previously melted size of the nanocrystals. For smaller nanocrystals a lower solidification temperature is observed in agreement with expectations from thermodynamic estimations of the critical grain size.

Acknowledgments

Financial support from MAT2004-04761 granted by MEC and from SGR2005-00201 by CIRIT is acknowledged. The authors are indebted to Prof. M.T. Clavaguera-Mora for useful discussions, Dr. F. Pi for the e-beam deposition and Dr. F.J. Muñoz from IMB-CNM for assistance in the microfabrication process. AFL thanks MEC for fellowships.

References

[1] S.S. Iyer, Y.H. Xie, Science 260 (1993) 40.
[2] K. Das, M. NandaGoswami, R. Mahapatra, G.S. Kar, A. Dhar, H.N. Acharya, S. Maikap, J.-H. Lee, S.K. Ray, Appl. Phys. Lett. 84 (2004) 1386.
[3] W.K. Choi, V. Ng, V.S.L. Swee, C.S. Ong, M.B. Yu, Rusli, S.F. Yoon, Scr. Mater. 44 (2001) 1873.
[4] W.K. Choi, H.G. Chew, F. Zheng, W.K. Chin, Y.L. Foo, E.A. Fitzgerald, Appl. Phys. Lett. 89 (2006) 113126.
[5] J. Solis, J. Siegel, C.N. Afonso, J. Jimenez, C. Garcia, J. Appl. Phys. 82 (1997) 236.
[6] P. Pawlow, Z. Phys. Chem. Stoechiom. Verwandtschaftsl. 65 (1909) 545.
[7] M. Takagi, J. Phys. Soc. Jpn. 9 (1954) 959.
[8] P.A. Buffat, J.P. Borel, Phys. Rev. A 13 (1976) 2287.
[9] A.N. Goldstein, C.M. Echer, A.P. Alivisatos, Science 256 (1992) 1425.
[10] A.N. Goldstein, Appl. Phys. A 62 (1996) 331.
[11] M. Zhang, M.Y. Efremov, F. Schiettekatte, E.A. Olson, A.T. Kwan, S.L. Lai, T. Wisleder, J.E. Greene, L.H. Allen, Phys. Rev. B 62 (2000) 10548.
[12] K. Lu, Z.H. Jin, Curr. Opin. Sol. State Mater. Sci. 5 (2001) 39.
[13] S.H. Yang, R.J. Berry, Mater. Res. Soc. Proc. 769 (2003) 201.
[14] H.W. Chiu, C.N. Chervin, S.M. Kauzlarich, Chem. Mater. 17 (2005) 4858.
[15] Q. Xu, I.D. Sharp, C.W. Yuan, D.O. Yi, C.Y. Liao, A.M. Glaeser, A.M. Minor, J.W. Beeman, M.C. Ridgway, P. Kluth, J.W. Ager III, D.C. Chrzan, E.E. Haller, Phys. Rev. Lett. 97 (2006) 155701.
[16] R. Srinivasan, I.M. Hsing, P.E. Berger, K.F. Jensen, S.L. Firebaugh, M.A. Schmidt, M.P. Harold, J.J. Lerou, J.F. Ryley, AIChE J. 43 (1997) 3059.
[17] D.W. Denlinger, E.N. Abarra, K. Allen, P.W. Rooney, M.T. Messer, S.K. Watson, F. Hellman, Rev. Sci. Instrum. 65 (1994) 946.
[18] L. Lai, G. Ramanath, L.H. Allen, P. Infante, Z. Ma, Appl. Phys. Lett. 67 (1995) 28.
[19] S.A. Adamovsky, A.A. Minakov, C. Schick, Thermochim. Acta 403 (2003) 55.
[20] O. Bourgeois, S. Skipetrov, F. Ong, J. Chaussy, Phys. Rev. Lett. 94 (2005) 057007.
[21] L. Lai, G. Ramanath, L.H. Allen, P. Infante, Z. Ma, Phys. Rev. Lett. 77 (1996) 99.
[22] A.T. Kwan, M.Y. Efremov, E.A. Olson, F. Schiettekatte, M. Zhang, P.H. Geil, L.H. Allen, J. Polym. Sci. B 39 (2001) 1237.
[23] A.F. Lopeandía, E. León-Gutierrez, F.J. Muñoz, J. Rodríguez-Viejo, Microelectron. Eng. 84 (2007) 1288.
[24] A.F. Lopeandía, J. Rodríguez-Viejo, M. Chacón, M.T. Clavaguera-Mora, F.J. Muñoz, J. Micromech. Microeng. 16 (2006) 1.
[25] M.Y. Efremov, E.A. Olson, M. Zhang, S. Lai, F. Schiettekatte, Z.S. Zhang, L.H. Allen, Thermochim. Acta 412 (2004) 13.
[26] A.F. Lopeandía, J. Rodríguez-Viejo, unpublished results.
[27] A.F. Lopeandía, E. León-Gutierrez, G. Garcia, F. Pi, A. Bernardi, A.R. Goñi, M.I. Alonso, J. Rodríguez-Viejo, Mater. Sci. Semicond. Process. 9 (2006) 806.
[28] E.P. Donovan, F. Spaepen, D. Turnbull, J.M. Poate, D.C. Jacobson, J. Appl. Phys. 57 (1985) 1795.
[29] A. Karmous, I. Berbezier, A. Ronda, Phys. Rev. B 73 (2006) 075323.